Published in final edited form as:
Cancer Res. 2019 June 15; 79(12): 3112–3124. doi:10.1158/0008-5472.CAN-18-3340.

Positron Emission Tomography Detects *In Vivo* Expression of Disialoganglioside GD2 in Mouse Models of Primary and Metastatic Osteosarcoma

Elizabeth R. Butch[1], **Paul E. Mead**[2], **Victor Amador Diaz**[1], **Heather Tillman**[2], **Elizabeth Stewart**[3], **Jitendra K. Mishra**[1,‡], **Jieun Kim**[6], **Armita Bahrami**[2], **Jason L.J. Dearling**[7,8], **Alan B. Packard**[7,8], **Shana V. Stoddard**[1,†], **Amy L. Vāvere**[1], **Yuanyuan Han**[4], **Barry L. Shulkin**[1], and **Scott E. Snyder**[1,5]

[1]Department of Diagnostic Imaging, St. Jude Children's Research Hospital, Memphis, TN 38105

[2]Department of Pathology, St. Jude Children's Research Hospital, Memphis, TN 38105

[3]Department of Oncology, St. Jude Children's Research Hospital, Memphis, TN 38105

[4]Department of Biostatistics, St. Jude Children's Research Hospital, Memphis, TN 38105

[5]Department of Chemical Biology & Therapeutics, St. Jude Children's Research Hospital, Memphis, TN 38105

[6]Center for In vivo Imaging and Therapeutics, St. Jude Children's Research Hospital, Memphis, TN 38105

[7]Division of Nuclear Medicine and Molecular Imaging, Department of Radiology, Boston Children's Hospital, Boston, MA 02115

[8]Department of Radiology, Harvard Medical School, Boston, MA 02115

Abstract

The cell membrane glycolipid GD2 is expressed by multiple solid tumors, including 88% of osteosarcomas and 98% of neuroblastomas. However, osteosarcomas are highly heterogeneous with many tumors exhibiting GD2 expression on <50% of the individual cells while some tumors are essentially GD2-negative. Anti-GD2 immunotherapy is the current standard of care for high-risk neuroblastoma, but its application to recurrent osteosarcomas, for which no effective therapies exist, has been extremely limited. This is in part because the standard assays to measure GD2 expression in these heterogeneous tumors are not quantitative and are subject to tissue availability and sampling bias. To address these limitations, we evaluated a novel, sensitive radiotracer [^{64}Cu]Cu-Bn-NOTA-hu14.18K322A to detect GD2 expression in osteosarcomas (six patient-derived xenografts and one cell line) *in vivo* using positron-emission tomography (PET). Tumor uptake of the radiolabeled, humanized anti-GD2 antibody [^{64}Cu]Cu-Bn-NOTA-hu14.18K322A

Corresponding Author: Scott E. Snyder, 262 Danny Thomas Place, Mail Stop 220, St Jude Children's Research Hospital, Memphis, TN 38105, 901-595-2008, 901-595-3981, Scott.snyder@stjude.org.
[‡] Author current affiliation: MilliporeSigma, Sheboygan Falls, WI 53085
[†] Author current affiliation: Department of Chemistry, Rhodes College, Memphis, TN 38112

Disclosure statement: The authors have no significant conflicts of interest

was 7-fold higher in modestly GD2-expressing osteosarcomas (32% GD2-positive cells) than in a GD2-negative tumor (9.8% *versus* 1.3% of the injected dose per cc, respectively). This radiotracer also identified lesions as small as 29 mm^3 in a 34% GD2-positive model of metastatic osteosarcoma of the lung. Radiolabeled antibody accumulation in patient-derived xenografts correlated with GD2 expression as measured by flow cytometry (Pearson $r = 0.88$, $p = 0.01$), distinguishing moderately GD2-expressing osteosarcomas (32-69% GD2-positive cells) from high GD2-expressors (>99%, $p < 0.05$). These results support the utility of GD2 imaging with PET to measure GD2 expression in osteosarcoma and thus maximize the clinical impact of anti-GD2 immunotherapy.

Keywords

GD2; osteosarcoma; imaging; immunotherapy; positron emission tomography

Introduction

The disialoganglioside GD2 is a cell-surface glycolipid involved in cell adhesion that is widely expressed by pediatric solid tumors (1) including osteosarcomas (2,3) and neuroblastomas (4,5). GD2 expression in normal tissue is limited to sympathetic neurons, skin melanocytes and peripheral sensory nerve fibers (6–9). Tumor GD2 expression is linked to increased cell migration and invasion (10), and there is some evidence of GD2 up-regulation in metastatic disease relative to the primary lesion (3). The intimate involvement of GD2 in disease progression and minimal expression in most non-neoplastic tissues make GD2 an attractive target for both immunotherapy (11–13) and imaging (1,5,14–16) that address the compelling clinical need to improve the outcomes of these patients.

Researchers have examined two murine IgG3 anti-GD2 antibodies for therapeutic efficacy in GD2-positive tumors (3): 3F8 and 14.18. Both antibodies as well as various analogs have been studied in multiple immunotherapy trials in patients with osteosarcoma, neuroblastoma and melanoma (1,12). A recent Children's Oncology Group (COG) trial that evaluated the chimeric antibody ch14.18 in patients with high-risk neuroblastoma demonstrated a 20% increase in two-year event-free survival (9). This is a substantial therapeutic improvement in a population with heretofore only 40-50% two-year disease-free survival (4,5). Based on the COG results and previous clinical experience, ch14.18 (dinutuximab, Unituxin®) was recently approved for the treatment of high-risk neuroblastoma.

Osteosarcomas are the most common bone tumor in children and young adults (17), and GD2 has been detected in >88% of these tumors (2,3). The overall survival rate for patients with recurrent osteosarcoma is less than 20% with no significant therapeutic improvements since the 1980s (17). Thus, there is a clear unmet need for new osteosarcoma therapies. This has led to an ongoing COG-sponsored trial investigating the utility of ch14.18 and cytokine therapy in recurrent osteosarcoma (17).

Although GD2 is nearly ubiquitous in osteosarcoma (2,3) and neuroblastoma (6,7), its expression level is highly variable, (3,12,18–20). Terzic *et al.* demonstrated a correlation between the variability in GD2 expression and response to ch14.18 treatment in neuroblastoma (20) leading researchers to hypothesize that differences in GD2 expression, both between patients and within a given tumor, may contribute to variations in immunotherapy response (21).

One study reported higher GD2 expression in recurrent osteosarcomas compared to initial biopsy (3), whereas another observed no difference between primary and recurrent osteosarcoma sites (19). One reason for this discordance may be that current *in vitro* GD2 assays are highly dependent on tumor sampling (19,20), tissue processing [the gangliosides are soluble in some solvents used to fix tissue (22)], and operator interpretation. Detection of GD2 expression by immunohistochemistry (IHC) is widely used and is reported to be more sensitive and accurate than flow cytometry (23). There are, however, inconsistencies in the IHC-measured GD2 levels for various cell lines and tumor types, and reports vary as to whether samples analyzed as touch preparations, fresh-frozen tissue, or paraffin-embedding provide consistent results (7,22). Likewise, flow cytometry can be challenging for clinical samples because of limited tissue availability. Detection of GD2 in blood (7) or bone marrow (24) samples obviates the limitations of biopsy, but does not provide information about the GD2 status of individual tumors. The challenging *in vitro* measurement of GD2 expression combined with the probable value of GD2 as a prognostic biomarker and the critical need to improve therapeutic outcomes creates an unmet clinical need for a method to measure GD2 expression *in situ* before treatment with anti-GD2 antibodies.

Positron emission tomography (PET) using a radiolabeled anti-GD2 antibody offers a potential non-invasive, quantitative method for initial staging, for informing treatment decisions, and for predicting therapeutic response for osteosarcoma patients. It also offers a method for identifying GD2-positive primary and metastatic tumors, thus allowing evaluation of disease progression and surveillance. Imaging-based screening protocols would maximize the clinical impact of anti-GD2 immunotherapy and aid in monitoring response to the various combinations of drug, antibody, cell cycle checkpoint inhibitors or immunomodulatory agents currently being evaluated for the treatment of osteosarcoma (25).

The 3F8, 14.G2a and ch14.18 anti-GD2 antibodies have been radiolabeled previously with ^{99m}Tcand radioiodine for imaging (16,26–30). These studies demonstrated the utility of qualitative GD2 imaging for earlier detection of skeletal and soft-tissue metastases. In addition, post-therapy images revealed that the GD2 binding was not saturated by therapeutic dosing with unlabeled antibody (16) indicating that imaging can be performed at multiple stages throughout therapy. More recently, studies demonstrated the feasibility of radiolabeling 14G.2a, ch14.18 (15) and hu14.18K322A (14) with ^{64}Cu as well as providing preliminary PET imaging results in strongly GD2-positive mouse models of neuroblastoma and melanoma. A subsequent study with ch14.18-CH2, examining the effect of chelators on biodistribution, reported that *S*-2-benzyl-1,4,7-triazacyclononane-1,4,7-triacetic acid (Bn-NOTA) chelator conjugated to the antibody *via* a thiourea linkage provided the optimum signal-to-noise profile (31).

We report here the first preclinical assessment of the PET radiotracer [^{64}Cu]Cu-Bn-NOTA-hu14.18K322A. The anti-GD2 antibody hu14.18K322A is the 98% humanized derivative of the murine 14.18 antibody, which has also shown great promise for immunotherapy of GD2-

positive tumors (32,33). This hu14.18 analog contains a single point-mutation in the CH2 domain (lysine-322 to alanine), resulting in fewer complement activation-dependent side-effects but with therapeutic potency comparable to the clinically approved ch14.18 (32,34–36). The bi-phasic pharmacokinetics of hu14.18K322A are similar to those of ch14.18 and other clinically used full-length IgG1_κ monoclonal antibodies ($t_{1/2}\alpha$ =1.74 days; $t_{1/2}\beta$ =21.1 days) (32).

Our results demonstrate an *in vivo* correlation between [^{64}Cu]Cu-Bn-NOTA-hu14.18K322A accumulation and GD2 expression in patient-derived osteosarcoma xenografts. We also demonstrate the ability of this new radiotracer to detect small GD2-positive lesions in even a modestly GD2-expressing mouse model of osteosarcoma metastasis to the lung, a key criterion for staging patients with osteosarcoma (37). These preclinical data also demonstrate that heterogeneous GD2 expression in primary and metastatic osteosarcoma can be examined non-invasively using PET. Such quantitative imaging allows *in situ* interrogation of the entire volume of each tumor in a given patient, and surveillance of changes at all sites of disease throughout therapy. This could significantly improve patient selection for anti-GD2 immunotherapy and serve as an *in vivo* probe for investigating the correlation between target expression and therapeutic response.

Materials and Methods

General

All chemicals and reagents were purchased from Sigma Chemical Co. unless noted otherwise. The hu14.18K322A antibody was provided by Children’s GMP, LLC, and is based on an expression construct licensed from EMD Sorono (a subsidiary of Merck KGaA). Copper-64 was purchased from The Mallinckrodt Institute of Radiology Cyclotron Facility, Washington University Medical Center. Distilled, deionized water (Milli-Q Integral Water Purification System, Millipore; 18.2 MΩ·cm resistivity) was used for all solutions. A CRC-15R dose calibrator (Capintec) or a Wizard^2 3 automatic γ-counter (PerkinElmer) was used to measure radioactivity in samples. All animal experiments were performed in compliance with St. Jude Children’s Research Hospital (St. Jude) Institutional Animal Care and Use Committee guidelines using approved protocols. The St. Jude animal program is accredited by the Association for the Assessment and Accreditation of Laboratory Animal Care Institutions (00429).

Antibody labeling

Conjugation of hu14.18K322A (4 mg/mL in 0.1 M sodium bicarbonate, pH 9.0) with 2-*S*-(4-isothiocyanatobenzyl)-1,4,7-triazacyclononane-1,4,7-triacetic acid (*p*-SCN-Bn-NOTA; Macrocyclics, Cat#B-605) was performed at a molar ratio of 10:1 (chelator:antibody) by the method of Vosjan *et al.* (31,38). The conjugation solution was incubated at 37°C for 40 min with gentle mixing. Unconjugated *p*-SCN-Bn-NOTA was removed by filtration through a PD-10 column (GE Healthcare) pre-equilibrated with 0.25 M sodium acetate, pH 5.5, followed by concentration by centrifugal filtration (Amicon Ultra-4, MWCO 30K, EMD Millipore, Cat#Z648035) to a final antibody concentration of 4 mg/mL for storage at −80°C until radiolabeling. The number of chelates per antibody molecule available for ^{64}Cu complexation was estimated by the isotopic dilution method (39) using [^{64}Cu]CuCl$_2$ diluted with non-radioactive CuCl$_2$ (31). The methods described here gave >98% pure Bn-NOTA-hu14.18K322A conjugate at 2-3 chelates/antibody.

Radiolabeling with ^{64}Cu was performed using 5 μCi/μg (185 Bq/μg) of antibody in 0.25 M sodium acetate, pH 5.5 (final antibody concentration 2 mg/mL) with gentle mixing for 40 min at 37°C. Labeling efficiency and radiochemical purity were determined using thin-layer chromatography as described previously (31). The final product had >95% radiochemical purity and 4-5 μCi/μg (145-185 Bq/μg) specific activity.

Cell culture

All cell lines were obtained through the American Tissue Culture Collection and all cell culture reagents were purchased from Invitrogen. Saos-2 (Cat#HTB-85, RRID:CVCL_0548) and U-2 OS (Cat#HTB-96, RRID:CVCL_0042) cell lines were grown in McCoy's 5A medium, HOS cells (Cat#CRL-1543, RRID:CVCL_0312) were grown in Eagle's Minimum Essential Medium and 143B cells (Cat#CRL-8303, RRID:CVCL_2270) were grown in Eagle's minimum essential medium in Earle's balanced salt solution with 0.015 mg/mL 5-bromo-2'-deoxyuridine. All media contained 10% FBS, and 1 mM *L*-glutamine. Cell lines were grown under humidified atmospheric conditions in 5% CO$_2$. All cell lines were verified mycoplasma-free (MycoAlert™, Lonza, Cat#LT07-418) and authenticated using short tandem repeat profiling (PowerPlex Fusion System, Promega, Cat#DC2408) immediately prior to use (2-3 weeks from thawing).

Patient-derived osteosarcoma xenografts

Human tumor tissue was obtained from patients with osteosarcoma through the Childhood Solid Tumor Network (St. Jude) and directly implanted into NOD *scid* gamma mice. Tumors were then propagated from mouse to mouse by sterile orthotopic implant (40). Immunocompromised NCr-*Foxn1*^{nu} mice were anesthetized (1.5-2.0% isoflurane) and the implant area was cleansed with alternating povidone iodine scrubs and 70% isopropyl alcohol wipes. A small horizontal incision was then made to insert a 100-125 mm^3 donor tumor piece, subcutaneously, above the right rear flank. The incision site was then treated with penicillin/streptomycin solution (1-2 drops; 10,000 U/mL) and closed with tissue adhesive (1-2 drops; Vetbond™, 3M). Tumors were allowed to grow to at least 150 mm^3 before imaging.

Mouse lung metastasis model

Lentiviral-yellow fluorescent protein (YFP) luciferase-labeled human 143B osteosarcoma cells were suspended in Matrigel® (BD Biosciences, Cat#354234) at 1×10^5 cells/L and placed on ice. NCr-*Foxn1*^{nu} nude mice were anesthetized (1.5% isoflurane) and placed in the supine position (41). Gentle rotation of a 25-guage needle was used to pierce between the femoral condyles as the needle was advanced into the shaft of the femur, where 10 μL of cell suspension was deposited. Animals were allowed to recover and were monitored for tumor growth by physical examination of the implantation site and weekly whole-body bioluminescence imaging.

Flow cytometry

All antibodies were purchased from BD Biosciences unless otherwise stated. Osteosarcoma xenograft tissue was diced into small fragments (<1 mm^3) in sterile RPMI 1640 medium and disaggregated by incubation at 37°C for 45 min in 0.26 Wünsch Units/mL of Liberase™ TM (Roche). The enzymatic reaction was terminated by adding EDTA to a final concentration of 5 mM. Cells were filtered (70 µm) and washed three times with cold PBS containing 0.1% (w/v) bovine serum albumin (PBS/BSA). For antibody staining, live cells (10^6) were transferred to tubes containing 50 µL PBS/BSA and 5 µL non-specific serum. An antibody cocktail containing CD133-APC (Miltenyi Biotec, Cat#130-090-826, RRID:AB_244340) and CD117-BV421 (Cat#562434, RRID:AB_11154222) tumor/stem cell markers, CD45-Alexa Fluor 700 leukocyte marker (BioLegend, Cat#304024, RRID:AB_493761), β2-microglobulin (Cat#551338, RRID:AB_394153) or HLA-ABC-FITC (Cat#555552, RRID:AB_395935) human-specific antigens, and either 14.G2a-PE anti-GD2 murine antibody (Cat#562100, RRID:AB_11154036) or isotype-matched IgG-PE control (Cat#555574, RRID:AB_395953) was added to each tube. After 10 min at ambient temperature, the cells were washed twice and resuspended in 400 µL PBS/BSA. A live/dead marker (Draq 7; Abcam, Cat#ab109202) was added before data collection on an LSRFortessa™ cytometer (BD Biosciences). Cells were gated for single, viable cells that expressed human cell surface markers (HLA-ABC or 2M) and were negative for CD45.

Histology and immunohistochemistry

Osteosarcoma patient-derived xenograft tumors were resected, embedded in optimal cutting temperature (OCT) compound (Sakura Tissue-Tek, Cat#4583), snap-frozen in liquid nitrogen and stored at −20°C. For the 143B osteosarcoma lung metastasis model, the liver, lungs and the 143B cell-engrafted hind limb were collected from each mouse and either snap-frozen or processed for formalin-fixed paraffin embedding (FFPE; 10% neutral buffered formalin) and sectioning. Snap-frozen tissues were embedded in OCT media, serial sections (8 µm) were cut and mounted onto positively charged glass slides (Superfrost Plus; ThermoFisher Scientific) and stained with hematoxylin & eosin (H&E) using an automated stainer (Dako). FFPE tissues were sectioned (4 µm), dried at 60°C for 20 min before dewaxing and staining with H&E. All H&E-stained tissues were evaluated for the extent of neoplastic engraftment by a board-certified veterinary pathologist to confirm the presence and morphologic phenotype of the primary xenograft and for evaluation of any metastatic disease in the sampled tissues.

Serial sections taken from both FFPE and snap-frozen specimens were labeled with 14.G2a anti-GD2 disialoganglioside antibody (1:500 dilution; BD Biosciences, Cat#554272, RRID:AB_395336), and counterstained with hematoxylin (IntelliPath FLX; Biocare Medical). These IHC sections were analyzed by two pathologists for the presence or absence of GD2 expression using an Eclipse Ni microscope (Nikon).

Bioluminescence imaging

In vivo bioluminescence imaging of luciferase-expressing 143B cells was performed using an IVIS-200 imaging system (PerkinElmer). Mice were injected intraperitoneally with *D*-luciferin (PerkinElmer) at 100 mg/kg body weight. After 3-5 min, the animals were anesthetized (2% isoflurane), and ventral and dorsal images were acquired using 1 min exposures with small binning and exposure adjustment when the signal was saturated. Data were analyzed using Living Image 4.5 software (PerkinElmer).

Magnetic resonance imaging

Magnetic resonance imaging (MRI) was performed using a 7-Tesla Brüker ClinScan small-animal MRI scanner (Brüker BioSpin MRI, GmbH) equipped with a Brüker 12S gradient and a two-channel phased-array surface coil. Animals were anesthetized (2-3% isoflurane) and double-gated (for respiration and cardiac motion) gradient-echo protocols (TR 411 ms; TE 3 ms) were used to produce lung images (coronal and axial) using a 176 × 256 matrix, 20 × 30 mm field of view (FOV), and a slice thickness of 0.6 mm. All images were analyzed on a Siemens workstation using Syngo MR B15 software (Siemens).

Small animal PET-CT

Small-animal PET, with computed tomography (CT) for attenuation correction, was performed on an Inveon system (Siemens Medical Solutions) using proprietary Inveon Research Workspace data analysis software with OSEM 3D reconstruction. Tumor-bearing mice were anesthetized (1.5-2% isoflurane), injected retro-orbitally (*r.o.*) with [^{64}Cu]Cu-Bn-NOTA-hu14.18K322A [65-80 μCi (2.4-3.0 MBq) in 100 μL] and allowed to recover. At 48 h post-injection, mice were anesthetized and single-position, whole-body, 20 min static PET images were acquired followed by a low-resolution CT scan (250 ms exposure with two bed positions and 36% overlap, 120 projections with FOV 54 × 133 mm) for anatomical co-registration and attenuation correction of the PET data. Tumor and non-target tissue regions of interest were drawn on the CT images and transferred to the PET images to calculate radioactivity concentration (percent of the injected dose/cubic centimeter, %ID/cc).

Ex vivo biodistribution

Osteosarcoma tumor-bearing NCr-*Foxn1^{nu}* nude mice (n =5-6 per tumor type) were anesthetized (1.5-2% isoflurane) and injected *r.o.* with 75 μCi (2.4-3.0 MBq, 100μL) of [^{64}Cu]Cu-Bn-NOTA-hu14.18K322A formulated in isotonic saline. At 48 h post injection, animals were anesthetized and euthanized by decapitation. Tissues were dissected, weighed and counted for radioactivity. Data were calculated as the percentage of injected dose per gram of wet tissue (%ID/g).

Results

GD2-positive osteosarcoma patient-derived xenografts (PDXs) are selectively detected by PET

We and others have demonstrated highly selective PET imaging of GD2 in neuroblastoma and melanoma (14,15). However, osteosarcoma imaging is rendered more difficult due to the inherent heterogeneity, calcification and variable incorporation of stromal cells in osteosarcoma tumors (42). The goal of this study was not only to demonstrate detection of these heterogeneous GD2-positive tumors, but also to characterize GD2 expression *in vivo*. We imaged immunocompromised (NCr-*Foxn1^{nu}*) mice bearing osteosarcoma PDXs using [^{64}Cu]Cu-Bn-NOTA-hu14.18K322A and PET. At 48 h post-injection, most of the unbound

[^{64}Cu]Cu-Bn-NOTA-hu14.18K322A had cleared from non-target tissue and only the strongly GD2-positive SJOS072 PDX tumor (>99% GD2-positive cells by flow cytometry, Table 1) and diffuse thoracic radioactivity were visible on the images (Figure 1A). Mean tumor radioactivity accumulation in the SJOS072 tumor was 11.4% ID/cc. A second, modestly GD2-positive PDX (SJOS051, 69% GD2-positive) also showed specific accumulation of radiotracer (Figure 1B) to 9.1% ID/cc.

For a more detailed characterization of the radiotracer distribution, we injected additional SJOS072 and SJOS051 PDX tumor-bearing mice with [^{64}Cu]Cu-Bn-NOTA-hu14.18K322A and euthanized them at 48 hours post-injection for dissection and tissue radioactivity assay. As observed in the PET data, the average tumor concentration of the tracer in SJOS072 (21 ±5.0% ID/g) and SJOS051 (8.3 ±1.9% ID/g) was proportional to tumor GD2 expression (Figure 1C), demonstrating selective accumulation of radiotracer in the GD2-positive osteosarcoma *versus* other tissues. The ^{64}Cu concentration in the blood at 48 h was still relatively high (8.7 ±4.5% and 7.3 ±1.6% ID/g, respectively) due to the 1.74-day biological half-life of hu14.18K322A (32) possibly combined with specific binding to circulating GD2 shed from tumors (7,24). The concentration of ^{64}Cu in liver (the primary metabolic organ) was ≤5% ID/g, indicating minimal loss of ^{64}Cu from the conjugate and similar to the ^{64}Cu concentration in all other non-target organs. As expected for a full-length IgG, we did not observe significant brain accumulation of radioactivity (<0.3% ID/g). These data indicate that [^{64}Cu]Cu-Bn-NOTA-hu14.18K322A exhibits highly selective accumulation in GD2-positive osteosarcomas and can easily detect tumors *in vivo* even at modest (69%) antigen expression levels.

PET can detect differences in GD2 expression in osteosarcoma PDXs

The different concentrations of [^{64}Cu]Cu-Bn-NOTA-hu14.18K322A in the SJOS051 and SJOS072 PDX osteosarcomas (Figure 1) suggested that we could use this radiotracer to measure tumor GD2 expression levels *in vivo*. To test this hypothesis, we determined the GD2 expression in six osteosarcoma PDX tumor types using IHC and flow cytometry and compared these data to the [^{64}Cu]Cu-Bn-NOTA-hu14.18K322A concentration in the same tumors measured by PET. Five of the six osteosarcoma PDXs exhibited varying degrees of GD2 expression by IHC (Figure 2A–2E). GD2 was not detected in the SJOS845 PDX sample (Figure 2F).

Further analysis by flow cytometry demonstrated a broad range of GD2 expression in these PDX tissues (Figure 2G–2L) and in four osteosarcoma cell lines, U-2 OS, Saos-2, HOS and 143B, (Figure 2M–2P, respectively and Table 1). The SJOS071 (Figure 2G) and SJOS072 (Figure 2H) PDX samples each exhibited >99% GD2-positive cells; however, their mean fluorescence intensity differed more than 10-fold (Table 1) reflecting a marked variance in the amount of GD2 on the cell surface. The percent GD2-positive cells in SJOS051, SJOS081 and SJOS121 (Figures 2I–2K) ranged from 32 to 69%. Consistent with the IHC results, SJOS845 (Figure 2L) was essentially GD2-negative, displaying <1% GD2-positive cells (Table 1). U-2 OS cells (Figure 2M) strongly express GD2 (10), whereas Saos-2 cells (Figure 2N) have minimal GD2 expression, and thus served as positive and negative controls, respectively, for the flow cytometry analyses.

We grew all six PDXs as flank tumors and imaged them by PET-CT using [^{64}Cu]Cu-Bn-NOTA-hu14.18K322A. Due to the heterogeneous nature of osteosarcoma tumors, we calculated the radioactivity concentration as both the mean concentration across the whole tumor volume ($PET_{(mean)}$) and the maximum concentration area within the tumor ($PET_{(max)}$), reporting the values as %ID/cc. As shown in Figure 3A, we observed a strong correlation (Pearson $r = 0.88$, $p = 0.01$) between the tumor radioactivity concentration in each of the six osteosarcoma PDXs measured by PET and the percentage of GD2-positive cells measured by flow cytometry, supporting the utility of PET imaging to evaluate GD2 in osteosarcoma. A higher linear correlation would not be expected, as osteosarcomas contain varying proportions of bone, cartilage, osteoid and fibrous tissue, in addition to other stromal and inflammatory cells (42).

The SJOS071 and SJOS072 PDXs had the highest uptake of [^{64}Cu]Cu-Bn-NOTA-hu14.18K322A, consistent with the >99% GD2 expression determined by flow cytometry. Conversely, SJOS845 (<1% GD2-positive) showed minimal [^{64}Cu]Cu-Bn-NOTA-hu14.18K322A accumulation and, as expected, was not discernable above normal background by PET. However, SJOS845 was a single sample whose propagation was unreliable and required 7-8 months, thus limiting its availability during the time frame of this study. Because additional GD2-negative PDXs were not available, the low GD2-expressing HOS osteosarcoma cell line (6.5% GD2-positive cells, Figure 2O) was examined for comparison (10). PET imaging of HOS flank tumors showed ^{64}Cu concentrations ($PET_{(mean)} = 7.2 \pm 1.2$ %ID/cc) comparable to blood levels but slightly higher than expected for non-specific uptake *via* the enhanced permeability and retention (EPR) affect [approximately 5% ID/cc (14,43)], and higher than predicted by a strictly linear correlation (Figure 3A). Regardless, inclusion of the HOS tumor data in the PDX data analysis had minimal effect on the strength of the correlation between PET and GD2 expression (Pearson $r = 0.86$, $p < 0.01$).

PET could not distinguish between PDXs with GD2-positive cells in the 32-69% range. As the sample sizes were small, we grouped the PET data into high (SJOS071 and SJOS072), moderate (SJOS051, SJOS081 and SJOS121) and low (SJOS845) GD2-expressing tumors. We then used a two-tailed exact Wilcoxon rank-sum test to compare the median of the $PET_{(mean)}$ (Figure 3B) and $PET_{(max)}$ (Figure 3C) radioactivity concentrations in the moderate-expression tumor group (15 individual data points) with those of the highest expressers (7 data points). For $PET_{(mean)}$, there was no significant difference between the moderate- and high-expression groups ($p = 0.34$). However, the highest GD2-expressers displayed $PET_{(max)}$ [^{64}Cu]Cu-Bn-NOTA-hu14.18K322A concentration values that were significantly higher ($p < 0.05$) than those of the moderate GD2-expressing group.

The low GD2-expressing HOS tumors were easily distinguished ($p < 0.001$, Figures 3B,3C) from other GD2-expressing tumors. Likewise, there was a striking 7-fold difference in radiotracer accumulation between the GD2-negative SJOS845 PDX and the next highest GD2-expressing PDX (SJOS121, 44% GD2-positive). However, as SJOS845 was a single data point we did not include it in the statistical analysis.

We confirmed this correlation observed between radiotracer accumulation and GD2 expression using dissection and counting methods (Figure 1C and Supplemental Data, Figure S1). As expected, ^{64}Cu concentrations measured in resected tumors showed a linear correlation with the PET data (Pearson r =0.93, p =0.01). As was seen in the PET images, the high GD2-expressing tumors SJOS071 and SJOS072 were easily distinguishable from those with moderate GD2 expression (SJOS051, SJOS081 and SJOS121; p <0.001) (Figure 3D).

Thus, ^{64}Cu]Cu-Bn-NOTA-hu14.18K322A can distinguish between low, moderate and high GD2-expressing osteosarcomas across a wide gradient of GD2 expression on the cell surface. Analysis of the maximum radioactivity accumulation, PET$_{(max)}$, within these heterogeneous tumors would provide a more useful clinical assessment of GD2 activity.

PET can detect even modestly GD2-positive metastatic disease *in vivo*

The lungs are a major site of metastatic disease, and the primary source of mortality, in osteosarcoma (37). Therefore, we investigated the efficacy of PET using [^{64}Cu]Cu-Bn-NOTA-hu14.18K322A to detect lung lesions. We generated a murine model of metastatic osteosarcoma by injecting luciferase-expressing 143B cells into the femur marrow of mice (n=8) (41,44–46), which produces pulmonary metastases in 70 to 80% of the animals (45,47). This cell line exhibits intermediate GD2 expression (34% GD2-positive cells; Figure 2P, Table 1) which provides a more representative model for the detection limitations of PET. We then subjected tumor-bearing mice to weekly imaging sessions (see Supplementary Data, Figure S2), starting with bioluminescence imaging (BLI) of YFP-luciferase-labeled 143B cells to monitor primary tumor engraftment as well as the development of metastatic disease. Animals that were positive for lung metastases on BLI were scanned using MRI, and then injected *r.o.* with [^{64}Cu]Cu-Bn-NOTA-hu14.18K322A and imaged 48 h post-injection. These results are summarized in Supplementary Data Table S1.

A representative mouse that was BLI-positive for lung metastasis 18 days post-implant is shown in Figure 4A (yellow arrow). MRI of this mouse (Figure 4B) revealed sites of high contrast in both lungs that were suspicious for osteosarcoma (white arrows). The primary tumor from the injection of the 143B cells into the femoral marrow was clearly visible in the PET-CT image of this animal (Figure 4C, white arrow). Interestingly, radioactivity accumulation was also apparent in the area of the lungs and thoracic cavity (orange arrow). To verify that the signal in the lungs was metastatic disease rather than non-specific accumulation or residual blood radioactivity, we harvested, sectioned and examined the lungs using histology (H&E staining) and IHC staining for GD2. All lung lesions identified by PET (Figure 4D) co-registered with areas exhibiting morphology consistent with the primary tumor phenotype (Figure 4E) and stained positive for GD2 (Figure 4F). Notably, the smallest of these metastatic lesions clearly identified by PET represents a volume of only 29 mm^3.

At the conclusion of imaging or at 7 weeks post-implant of tumors, by which time the primary tumor size had progressed to the humane endpoint, we imaged and then euthanized all animals and confirmed suspected sites of disease by histology and IHC staining for GD2

(Figure 5). We confirmed engraftment at the primary injection site in seven of the eight animals by H&E staining. Figures 5A and 5B show an example of bone marrow engraftment and expansion of the tumor into the extramedullary muscle. GD2 staining of the primary tumor (Figure 5C) corresponded with the 34% GD2 expression determined by flow cytometry (Figure 2P and Table 1). We also confirmed disease in the lung in six mice, with morphology consistent with the primary tumor phenotype (Figure 5D). These metastatic sites also stained positive for GD2 expression (Figures 5E and 5F). MRI identified histology-confirmed lung lesions as small as approximately 1 mm^3. A histology-confirmed 12 mm^3 lung lesion was visible on both MRI and PET; however, the radiotracer accumulation in this lesion was not significantly above the blood levels in the pulmonary vessels. Those histology-confirmed lesions not seen on imaging consisted of neoplastic cells that individualized or formed small clusters in capillaries but lacked clear establishment within the lungs. These data confirm that the metastatic lesions identified by PET imaging were histologically identical to the primary osteosarcoma and were positive for GD2 by IHC staining. Thus, PET provides a non-invasive method to monitor extremely small osteosarcoma lesions in a clinically relevant lung metastasis model.

Discussion

In this study, we present the first preclinical assessment of a ^{64}Cu-labeled GD2 antibody in a metastatic osteosarcoma model and demonstrate *in vivo* correlation between radiotracer accumulation and GD2 expression in osteosarcoma PDXs. This novel quantitative imaging method bridges a critical gap in our ability to examine the frequency and intensity of GD2 expression in osteosarcoma, for which patients currently have limited access to the proven clinical benefits of anti-GD2 immunotherapy.

Osteosarcoma and other solid tumors are known to express cell-surface disialogangliosides, particularly GD2 and GD3 (10,11,19,48,49). Building on the therapeutic success of recent clinical trials of GD2-targeted immunotherapy in neuroblastoma (11,49), there is strong clinical interest in treatment protocols that include anti-GD2 immunotherapy for other malignancies, such as osteosarcoma, where GD2 expression is lower and/or less uniform than in neuroblastoma (17). Current *in vitro* methods for measuring GD2 expression (IHC, quantitative PCR and flow cytometry) are highly dependent on factors such as tumor sampling, tissue processing and operator interpretation, which could explain inconsistencies in reported GD2 levels (19,20,22). A PET-based assay of GD2 expression enables quantitative *in situ* interrogation of the entire tumor volume and allows surveillance of changes in all disease sites throughout the body.

We have shown that GD2-positive primary and metastatic osteosarcomas are readily detected using the novel PET radiotracer [^{64}Cu]Cu-Bn-NOTA-hu14.18K322A, which clearly visualized GD2 expression ranging from 32% to 100% of cells. Pearson analysis of a group of six subcutaneously implanted PDX tumors (Figure 3A) showed a strong correlation ($r = 0.88$, $p = 0.01$) between the radiotracer concentration and the flow cytometry data for these tumors.

Consistent with known osteosarcoma tumor heterogeneity, we observed larger than expected variations in the accumulation of [^{64}Cu]Cu-Bn-NOTA-hu14.18K322A in tumors within some PDX groups but not in the corresponding normal tissues. This variability could be due to histological heterogeneity of osteosarcomas or actual variation in the amount of GD2 expressed on cell surfaces within a given PDX and was particularly pronounced in the high GD2-expressing PDXs, SJOS071 and SJOS072 (Figures 3A and S1). Despite this variability, [^{64}Cu]Cu-Bn-NOTA-hu14.18K322A PET could clearly distinguish between high GD2-expressing (>99% GD2-positive; SJOS072 and SJOS071) and moderate GD2-expressing (32-69% GD2-positive; SJOS121, SJOS051 and SJOS081) osteosarcomas ($p < 0.05$) using the maximum radiotracer accumulation values (PET$_{(max)}$), which are less affected by tumor heterogeneity. We did not observe a difference by PET among the moderately GD2-expressing PDX group.

The low GD2-expressing HOS cell (6.5% GD2 expression) and SJOS0845 PDX (<1% GD2 expression) tumors had minimal radiotracer accumulation, and were easily distinguished ($p < 0.001$, Figure 3C) from other GD2-expressing tumors, despite the fact that the actual GD2 expression of the HOS cells is lower than predicted by PET (Figure 3A). This discrepancy could arise because the immortalized cell line produces more homogeneous tumors exhibiting a higher tumor cell density per gram than the PDX models. Likewise, the exceptionally low radiotracer accumulation in SJOS0845 is consistent with the high level of calcification observed in this PDX or could also be indicative of particularly low vascularization. However, the high blood radioactivity concentration and EPR effect limit quantification in this low GD2-expression range.

These data suggest that the PET$_{(max)}$ values are a better indicator of actual GD2 status than the PET$_{(mean)}$ accumulation values, and support using PET imaging to establish a clinical GD2 threshold below which patients are unlikely to respond to anti-GD2 immunotherapy.

Our primary goal is to develop a PET radiotracer for GD2 that can be rapidly translated to human use. Thus, we used the full-length hu14.18K322A antibody (already used in clinical studies) to prepare the corresponding ^{64}Cu-labeled radiotracer. A key advantage of ^{64}Cu in preclinical investigation is that it allows weekly imaging to evaluate therapy response and to examine the potential effect of pharmacological doses of GD2 antibodies and other therapeutic agents on the images. However, owing to the slow clearance of the full-length antibody [hu14.18K322A $t_{½}$=1.74 d (32)], possibly combined with specific binding of antibody to circulating ganglioside shed from the GD2-expressing tumors (7), the blood levels of [^{64}Cu]Cu-Bn-NOTA-hu14.18K322A observed at 48 h still exceed those in the major organs (Figure 1C). This residual radioactivity in the blood resulted in visualization of the major vessels on the images, which could confound the detection of metastatic lung lesions as well as potentially adding variability when quantifying images of well-vascularized tumors. Co-injection of [^{64}Cu]Cu-Bn-NOTA-hu14.18K322A with excess unmodified hu14.18K322A did not decrease the blood radioactivity levels at 48 hours ($p = 0.57$; Supplementary Data, Figure S3). Thus, anti-GD2 PET imaging demonstrates no saturable specific binding to GD2 in the blood and will not be adversely affected by therapeutic levels of anti-GD2 antibodies in patients undergoing immunotherapy.

In an effort to improve on the radiotracer pharmacokinetics of full-length antibodies, various groups have used protein engineering of antibody fragments to improve blood clearance (31,50). Alternatively, imaging challenges due to the slow antibody clearance could be addressed by using a radionuclide with a longer physical half-life. For example, several full-length antibodies labeled with ^{89}Zr ($t_{½}$ =78 h) rather than ^{64}Cu are currently used in clinical trials (38). The longer half-life of ^{89}Zr allows imaging 5-7 days (3-4 biological half-lives) after radiotracer injection, giving additional time for unbound radiotracer to clear. The disadvantage of ^{89}Zr is that images are not available until 5-7 days post-injection and sequential imaging is not possible for 14-20 days, to allow for clearance and decay of the ^{89}Zr from the initial injection. Also, development of ^{64}Cu-labeled antibodies such as [^{64}Cu]Cu-Bn-NOTA-hu14.18K322A for diagnostic imaging allows direct translation to use in radioimmunotherapy as the ^{64}Cu/^{67}Cu theranostic pair.

Our results show that despite this limitation, [^{64}Cu]Cu-Bn-NOTA-hu14.18K322A can distinguish lesions as small as 29 mm^3 from background even in a modestly GD2-positive (34% GD2-positive cells) model of metastatic osteosarcoma of the lung (Figure 4D). Interestingly, metastatic lesions in this model exhibited a higher ^{64}Cu concentration than did the primary lesion in the same animal (*e.g.*, 10.5% *versus* 8.5% ID/cc for the lung metastasis and primary tumor, respectively). Dearling *et al.* showed that the concentration of radiolabeled anti-GD2 antibody accumulating in tumors is inversely proportional to tumor size (51), and that lesions smaller than 100 mm^3 showed 2-3-fold higher accumulation of radiotracer compared to larger tumors. Roth *et al.* observed that metastatic sites often express levels of GD2 that are higher than those in the primary lesions (3). We found no discernable difference in GD2 expression of primary *versus* metastatic lesions by IHC (Figures 5C and 5F); however, and the priority for histopathological confirmation to validate the imaging results precluded cytometric analysis of GD2 expression in the resected tissues. Further examination will be required to determine which of these phenomena, dependence of the PET signal on tumor size or increased GD2 expression (or a combination of both), is responsible for the higher PET signal at the metastatic sites.

Our results demonstrate that PET imaging of GD2 expression can serve as a companion diagnostic method for anti-GD2 immunotherapy. PET imaging allows *in situ* assessment of GD2 expression in all sites of disease throughout therapy and could serve as a non-invasive, *in vivo* probe for investigating the relationship between target expression and therapeutic response. These studies also provide *in vivo* antibody distribution data that inform further development of anti-GD2 radioimmunotherapy, which has potential for treating minimal residual disease before these hidden clusters of cancer cells present as metastatic disease.

Supplementary Material

Refer to Web version on PubMed Central for supplementary material.

Acknowledgements

The authors thank Kimberly Guy and Adam Petraglia for animal assistance, Dr. Yimei Li for biostatistics consulting, and the Childhood Solid Tumor Network (St. Jude) and Dr. Chris Morton for supplying osteosarcoma xenograft mice and tissues. Special thanks are given to Drs. Raymond Barfield, Michael Bishop, Michael Dyer, Amos Loh and Fariba Navid for advice and multiple discussions on immunotherapy, and to the following St. Jude Shared Resources: the Center for *In Vivo* Imaging and Therapeutics (CIVIT), Biostatistics, and the Hartwell Center. Financial support for this work was provided by Cancer Center Support Grant P30 CA021765 (Developmental Project pilot funds to S. Snyder) and by American Lebanese Syrian Associated Charities (St Jude).

Financial Support: Support for this work was provided by a Development Projects Fund (SES) from Cancer Center Support Grant P30 CA021765 and by the American Lebanese Syrian Associated Charities (ALSAC)

References

1. Dobrenkov K and Cheung NK. GD2-targeted immunotherapy and radioimmunotherapy. Semin Oncol 2014;41:589–612. [PubMed: 25440605]
2. Heiner JP, Miraldi F, Kallick S, Makley J, Neely J, Smith-Mensah WH, et al. Localization of GD2-specific monoclonal antibody 3F8 in human osteosarcoma. Cancer Res 1987;47:5377–81. [PubMed: 3115567]
3. Roth M, Linkowski M, Tarim J, Piperdi S, Sowers R, Geller D, et al. Ganglioside GD2 as a therapeutic target for antibody-mediated therapy in patients with osteosarcoma. Cancer 2014;120:548–54. [PubMed: 24166473]
4. Brodeur GM. Neuroblastoma: biological insights into a clinical enigma. Nat Rev Cancer 2003;3:203–16. [PubMed: 12612655]
5. Kushner BH. Neuroblastoma: a disease requiring a multitude of imaging studies. J Nucl Med 2004;45:1172–88. [PubMed: 15235064]
6. Cheung NK, Saarinen UM, Neely JE, Landmeier B, Donovan D and Coccia PF. Monoclonal antibodies to a glycolipid antigen on human neuroblastoma cells. Cancer Res 1985;45:2642–9. [PubMed: 2580625]
7. Schulz G, Cheresh DA, Varki NM, Yu A, Staffileno LK and Reisfeld RA. Detection of ganglioside GD2 in tumor tissues and sera of neuroblastoma patients. Cancer Res 1984;44:5914–20. [PubMed: 6498849]
8. Svennerholm L, Bostrom K, Fredman P, Jungbjer B, Lekman A, Mansson JE, et al. Gangliosides and allied glycosphingolipids in human peripheral nerve and spinal cord. Biochim Biophys Acta 1994;1214:115–23. [PubMed: 7918590]
9. Yu AL, Gilman AL, Ozkaynak MF, London WB, Kreissman SG, Chen HX, et al. Anti-GD2 antibody with GM-CSF, interleukin-2, and isotretinoin for neuroblastoma. N Engl J Med 2010;363:1324–34. [PubMed: 20879881]
10. Shibuya H, Hamamura K, Hotta H, Matsumoto Y, Nishida Y, Hattori H, et al. Enhancement of malignant properties of human osteosarcoma cells with disialyl gangliosides GD2/GD3. Cancer Sci 2012;103:1656–64. [PubMed: 22632091]
11. Yang RK and Sondel PM. Anti-GD2 Strategy in the Treatment of Neuroblastoma. Drugs Future 2010;35:665. [PubMed: 21037966]
12. Ahmed M and Cheung NK. Engineering anti-GD2 monoclonal antibodies for cancer immunotherapy. FEBS Lett 2014;588:288–97. [PubMed: 24295643]
13. Horta ZP, Goldberg JL and Sondel PM. Anti-GD2 mAbs and next-generation mAb-based agents for cancer therapy. Immunotherapy 2016;8:1097–1117. [PubMed: 27485082]
14. Vavere AL, Butch ER, Dearling JL, Packard AB, Navid F, Shulkin BL, et al. ^{64}Cu-*p*-NH$_2$-Bn-DOTA-hu14.18K322A, a PET radiotracer targeting neuroblastoma and melanoma. J Nucl Med 2012;53:1772–8. [PubMed: 23064212]
15. Voss SD, Smith SV, DiBartolo N, McIntosh LJ, Cyr EM, Bonab AA, et al. Positron emission tomography (PET) imaging of neuroblastoma and melanoma with ^{64}Cu-SarAr immunoconjugates. Proc Natl Acad Sci U S A 2007;104:17489–93. [PubMed: 17954911]
16. Reuland P, Handgretinger R, Smykowsky H, Dopfer R, Klingebiel T, Miller BM, et al. Application of the murine anti-Gd-2 antibody 14.Gd-2a for diagnosis and therapy of neuroblastoma. Int J Rad Appl Instrum B 1991;18:121–5. [PubMed: 2010296]
17. Harrison DJ, Geller DS, Gill JD, Lewis VO and Gorlick R. Current and future therapeutic approaches for osteosarcoma. Expert Rev Anticancer Ther 2018;18:39–50. [PubMed: 29210294]

18. Gorlick R, Janewayk K and Marina N, Osteosarcoma In, Pizzo PA and Poplack DG, editors. Principles and Practices of Pediatric Oncology. Lippincott, Williams & Wilkins; 2016 p. 877–898.
19. Poon VI, Roth M, Piperdi S, Geller D, Gill J, Rudzinski ER, et al. Ganglioside GD2 expression is maintained upon recurrence in patients with osteosarcoma. Clinical Sarcoma Research 2015;5:4. [PubMed: 25642322]
20. Terzic T, Cordeau M, Herblot S, Teira P, Cournoyer S, Beaunoyer M, et al. Expression of Disialoganglioside (GD2) in Neuroblastic Tumors: A Prognostic Value for Patients Treated With Anti-GD2 Immunotherapy. Pediatr Dev Pathol 2018;21:355–362. [PubMed: 29067879]
21. Cheung NK and Dyer MA. Neuroblastoma: developmental biology, cancer genomics and immunotherapy. Nat Rev Cancer 2013;13:397–411. [PubMed: 23702928]
22. Sariola H, Terava H, Rapola J and Saarinen UM. Cell-surface ganglioside GD2 in the immunohistochemical detection and differential diagnosis of neuroblastoma. Am J Clin Pathol 1991;96:248–52. [PubMed: 1713742]
23. Ifversen MR, Kagedal B, Christensen LD, Rechnitzer C, Petersen BL and Heilmann C. Comparison of immunocytochemistry, real-time quantitative RT-PCR and flow cytometry for detection of minimal residual disease in neuroblastoma. Int J Oncol 2005;27:121–9. [PubMed: 15942651]
24. Corrias MV, Parodi S, Haupt R, Lacitignola L, Negri F, Sementa AR, et al. Detection of GD2-positive cells in bone marrow samples and survival of patients with localised neuroblastoma. Br J Cancer 2008;98:263–9. [PubMed: 18182983]
25. Sampson VB, Gorlick R, Kamara D and Anders Kolb E. A review of targeted therapies evaluated by the pediatric preclinical testing program for osteosarcoma. Front Oncol 2013;3:Article 132.
26. Cheung NK, Landmeier B, Neely J, Nelson AD, Abramowsky C, Ellery S, et al. Complete tumor ablation with iodine 131-radiolabeled disialoganglioside GD2-specific monoclonal antibody against human neuroblastoma xenografted in nude mice. J Natl Cancer Inst 1986;77:739–45. [PubMed: 3091900]
27. Miraldi FD, Nelson AD, Kraly C, Ellery S, Landmeier B, Coccia PF, et al. Diagnostic imaging of human neuroblastoma with radiolabeled antibody. Radiology 1986;161:413–8. [PubMed: 3763911]
28. Yeh SD, Larson SM, Burch L, Kushner BH, Laquaglia M, Finn R, et al. Radioimmunodetection of neuroblastoma with iodine-131-3F8: correlation with biopsy, iodine-131-metaiodobenzylguanidine and standard diagnostic modalities. J Nucl Med 1991;32:769–76. [PubMed: 1902508]
29. Daghighian F, Pentlow KS, Larson SM, Graham MC, DiResta GR, Yeh SD, et al. Development of a method to measure kinetics of radiolabelled monoclonal antibody in human tumour with applications to microdosimetry: positron emission tomography studies of iodine-124 labelled 3F8 monoclonal antibody in glioma. Eur J Nucl Med 1993;20:402–9. [PubMed: 8519259]
30. Reuland P, Geiger L, Thelen MH, Handgretinger R, Haase B, Muller-Schauenburg W, et al. Follow-up in neuroblastoma: comparison of metaiodobenzylguanidine and a chimeric anti-GD2 antibody for detection of tumor relapse and therapy response. J Pediatr Hematol Oncol 2001;23:437–42. [PubMed: 11878578]
31. Dearling JL, Paterson BM, Akurathi V, Betanzos-Lara S, Treves ST, Voss SD, et al. The ionic charge of copper-64 complexes conjugated to an engineered antibody affects biodistribution. Bioconjug Chem 2015;26:707–17. [PubMed: 25719414]
32. Navid F, Sondel PM, Barfield R, Shulkin BL, Kaufman RA, Allay JA, et al. Phase I Trial of a Novel Anti-GD2 Monoclonal Antibody, Hu14.18K322A, Designed to Decrease Toxicity in Children With Refractory or Recurrent Neuroblastoma. J Clin Oncol 2014;32:1445–52. [PubMed: 24711551]
33. Federico SM, McCarville MB, Shulkin BL, Sondel PM, Hank JA, Hutson P, et al. A Pilot Trial of Humanized Anti-GD2 Monoclonal Antibody (hu14.18K322A) with Chemotherapy and Natural Killer Cells in Children with Recurrent/Refractory Neuroblastoma. Clin Cancer Res 2017;23:6441–6449. [PubMed: 28939747]
34. Sorkin LS, Otto M, Baldwin WM 3rd, Vail E, Gillies SD, Handgretinger R, et al. Anti-GD_2 with an FC point mutation reduces complement fixation and decreases antibody-induced allodynia. Pain 2010;149:135–42. [PubMed: 20171010]

35. Thommesen JE, Michaelsen TE, Loset GA, Sandlie I and Brekke OH. Lysine 322 in the human IgG3 C(H)2 domain is crucial for antibody dependent complement activation. Mol Immunol 2000;37:995–1004. [PubMed: 11395138]
36. Navid F, Armstrong M and Barfield RC. Immune therapies for neuroblastoma. Cancer Biol Ther 2009;8:874–82. [PubMed: 19342881]
37. Bielack SS, Kempf-Bielack B, Delling G, Exner GU, Flege S, Helmke K, et al. Prognostic factors in high-grade osteosarcoma of the extremities or trunk: an analysis of 1,702 patients treated on neoadjuvant cooperative osteosarcoma study group protocols. J Clin Oncol 2002;20:776–90. [PubMed: 11821461]
38. Vosjan MJ, Perk LR, Visser GW, Budde M, Jurek P, Kiefer GE, et al. Conjugation and radiolabeling of monoclonal antibodies with zirconium-89 for PET imaging using the bifunctional chelate p-isothiocyanatobenzyl-desferrioxamine. Nat Protoc 2010;5:739–43. [PubMed: 20360768]
39. Meares CF, McCall MJ, Reardan DT, Goodwin DA, Diamanti CI and McTigue M. Conjugation of antibodies with bifunctional chelating agents: isothiocyanate and bromoacetamide reagents, methods of analysis, and subsequent addition of metal ions. Anal Biochem 1984;142:68–78. [PubMed: 6440451]
40. Stewart E, Federico S, Karlstrom A, Shelat A, Sablauer A, Pappo A, et al. The Childhood Solid Tumor Network: A new resource for the developmental biology and oncology research communities. Dev Biol 2016;411:287–293. [PubMed: 26068307]
41. Stewart E, Federico SM, Chen X, Shelat AA, Bradley C, Gordon B, et al. Orthotopic patient-derived xenografts of paediatric solid tumours. Nature 2017;549:96–100. [PubMed: 28854174]
42. Raymond AK and Jaffe N. Osteosarcoma multidisciplinary approach to the management from the pathologist’s perspective. Cancer Treat Res 2009;152:63–84. [PubMed: 20213386]
43. Maeda H Tumor-selective delivery of macromolecular drugs via the EPR effect: background and future prospects. Bioconjug Chem 2010;21:797–802. [PubMed: 20397686]
44. Berlin O, Samid D, Donthineni-Rao R, Akeson W, Amiel D and Woods VL Jr. Development of a novel spontaneous metastasis model of human osteosarcoma transplanted orthotopically into bone of athymic mice. Cancer Res 1993;53:4890–5. [PubMed: 8402677]
45. Luu HH, Kang Q, Park JK, Si W, Luo Q, Jiang W, et al. An orthotopic model of human osteosarcoma growth and spontaneous pulmonary metastasis. Clin Exp Metastasis 2005;22:319–29. [PubMed: 16170668]
46. Miretti S, Roato I, Taulli R, Ponzetto C, Cilli M, Olivero M, et al. A mouse model of pulmonary metastasis from spontaneous osteosarcoma monitored in vivo by Luciferase imaging. PLoS One 2008;3:e1828. [PubMed: 18350164]
47. Osaki M, Takeshita F, Sugimoto Y, Kosaka N, Yamamoto Y, Yoshioka Y, et al. MicroRNA-143 regulates human osteosarcoma metastasis by regulating matrix metalloprotease-13 expression. Mol Ther 2011;19:1123–30. [PubMed: 21427707]
48. Dobrenkov K, Ostrovnaya I, Gu J, Cheung IY and Cheung NV. Oncotargets GD2 and GD3 are highly expressed in sarcomas of children, adolescents, and young adults. Pediatr Blood Cancer 2016.
49. Suzuki M and Cheung NK. Disialoganglioside GD2 as a therapeutic target for human diseases. Expert Opin Ther Targets 2015;19:349–62. [PubMed: 25604432]
50. Mueller BM, Reisfeld RA and Gillies SD. Serum half-life and tumor localization of a chimeric antibody deleted of the CH2 domain and directed against the disialoganglioside GD2. Proc Natl Acad Sci U S A 1990;87:5702–5. [PubMed: 2198570]
51. Dearling JL, Voss SD, Dunning P, Snay E, Fahey F, Smith SV, et al. Imaging cancer using PET-the effect of the bifunctional chelator on the biodistribution of a ^{64}Cu-labeled antibody. Nucl Med Biol 2011;38:29–38. [PubMed: 21220127]

Significance:

In situ assessment of all GD2-positive osteosarcoma sites with a novel PET radiotracer could significantly impact anti-GD2 immunotherapy patient selection and enable non-invasive probing of correlations between target expression and therapeutic response.

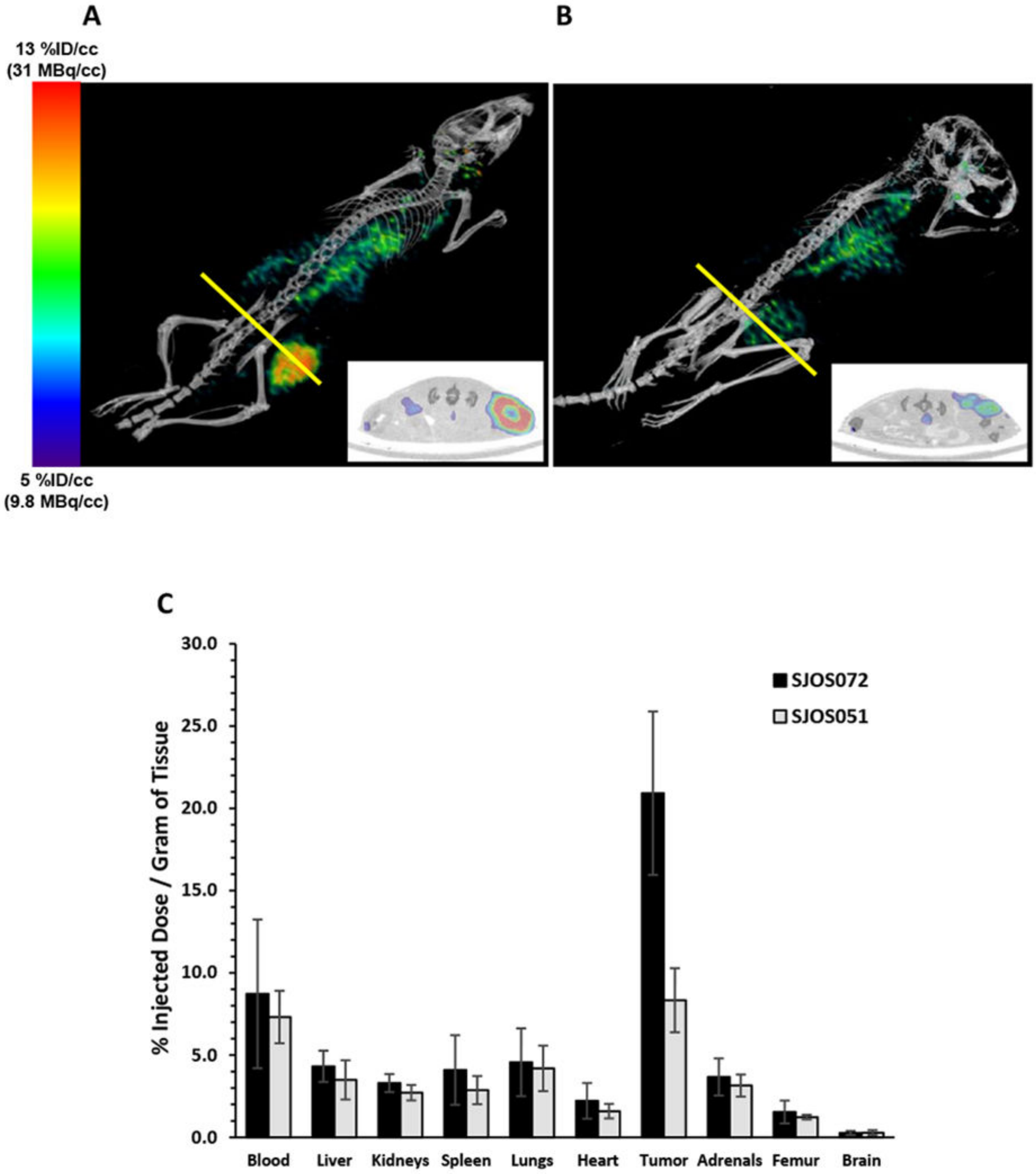

Figure 1.

Representative static 20 min small-animal PET-CT of nude mice bearing a *s.c.* flank SJOS072 (**A**) or SJOS051 (**B**) osteosarcoma xenograft imaged at 48 h post-injection of [^{64}Cu]Cu-Bn-NOTA-hu14.18K322A. We have reported previously (14) that imaging of ^{64}Cu-labeled hu14.18K322A antibodies at 48 hours post-injection provided the optimum balance between the physical half-life of the radionuclide (12.7 h) and the biological clearance half-life of the antibody ($t_{1/2}\alpha$ = 1.74 d) Panels **A** and **B** are intensity matched to a scale of 9.8-31 MBq per cc. Tumor region of interest was drawn on the CT image and transferred to the PET image for calculation of the tumor radioactivity concentration (%ID/cc). Inset in panels **A** and **B** are cross-sections through the largest transverse diameter of the tumor (yellow line). Tumor $\mathrm{PET}_{(\mathrm{mean})}$ radioactivity concentrations from these images are 11.4 and 9.1% ID/cc for mice **A** and **B**, respectively. **C**. *Ex vivo* biodistribution of [^{64}Cu]Cu-Bn-NOTA-hu14.18K322A in SJOS072 (n=6) and SJOS051 (n=5) tumor-bearing nude mice at 48 hours post-injection of radiotracer. Groups of mice were euthanized, dissected and tissues counted for radioactivity in an automated gamma counter. Data are presented as the percent of injected dose per gram of wet tissue (mean %ID/g ± standard deviation). Radiotracer concentration in each of the non-target tissues was less than blood concentration (p <0.05, unpaired, one-tailed Student's t-test) in all 5 different osteosarcoma PDX models (see Supplementary Data Figure S1).

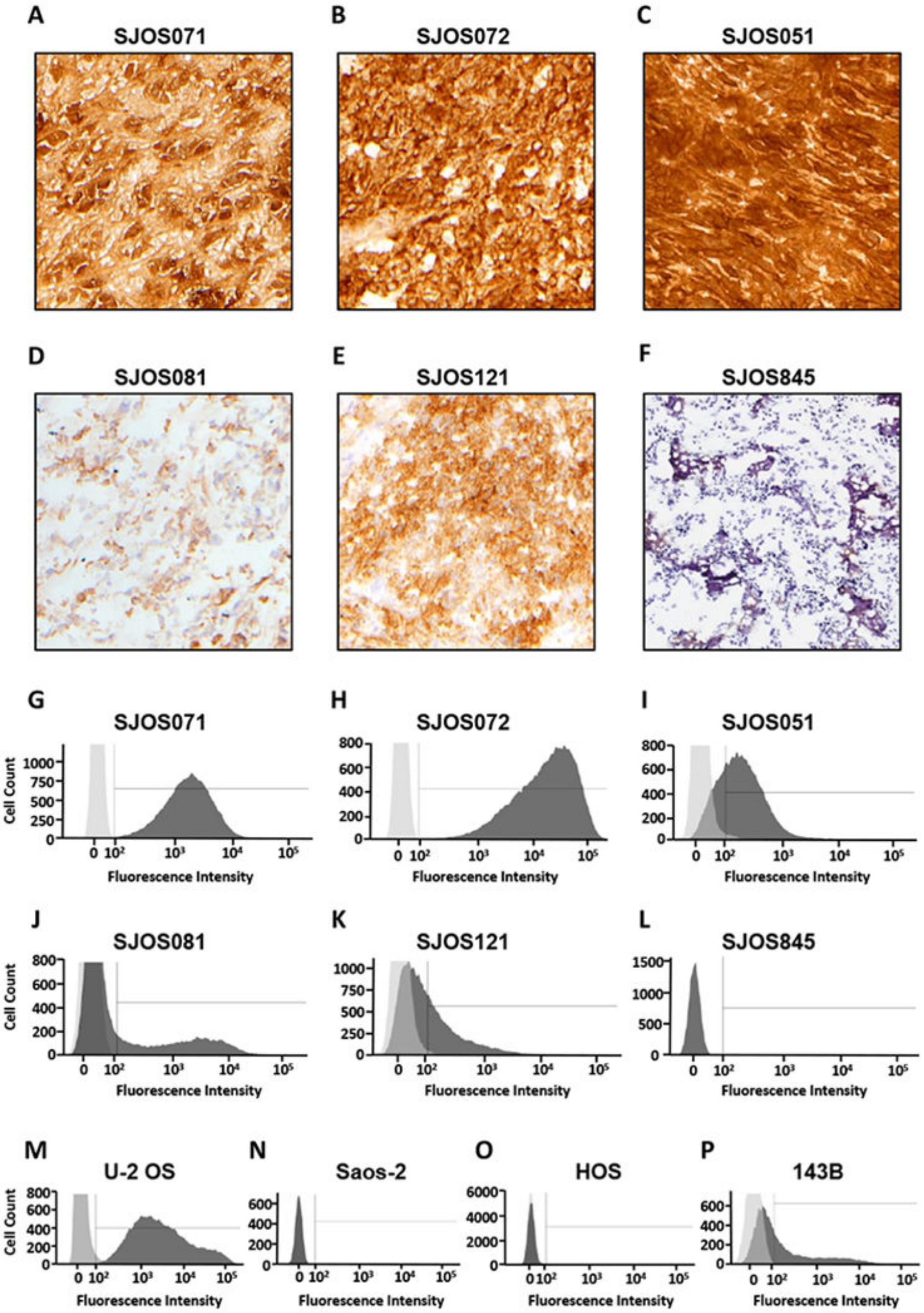

Figure 2.

GD2 expression measured *in vitro* by IHC and flow cytometry varies in osteosarcoma PDXs and cell lines. Immunohistochemical staining with purified mouse anti-human GD2 antibody 14.G2a (counterstained with hematoxylin) of osteosarcoma PDX (**A**) SJOS071, (**B**) SJOS072, (**C**) SJOS051, (**D**) SJOS081, (**E**) SJOS121 and (**F**) SJOS845 tumors. Panels **G-L** display the corresponding flow cytometry analysis on (**G**) SJOS071, (**H**) SJOS072 and (**I**) SJOS051, (**J**) SJOS081, (**K**) SJOS121 and (**L**) SJOS845 osteosarcoma PDX tumors (dark grey) and isotype control (light grey) selecting for single, viable cells that express human cell surface markers. Panels **M-P** show the histograms for osteosarcoma cell lines (**M**) U-2 OS, (**N**) Saos-2, (**O**) HOS and (**P**) 143B. Histograms for the GD2-negative PDX, SJOS845 (**F**), and the Saos-2 cell line (**N**) completely overlap with the antibody isotype control. The HOS cell histogram (**O**) has a long, low intensity tail that corresponds to 6.5% GD2 expression.

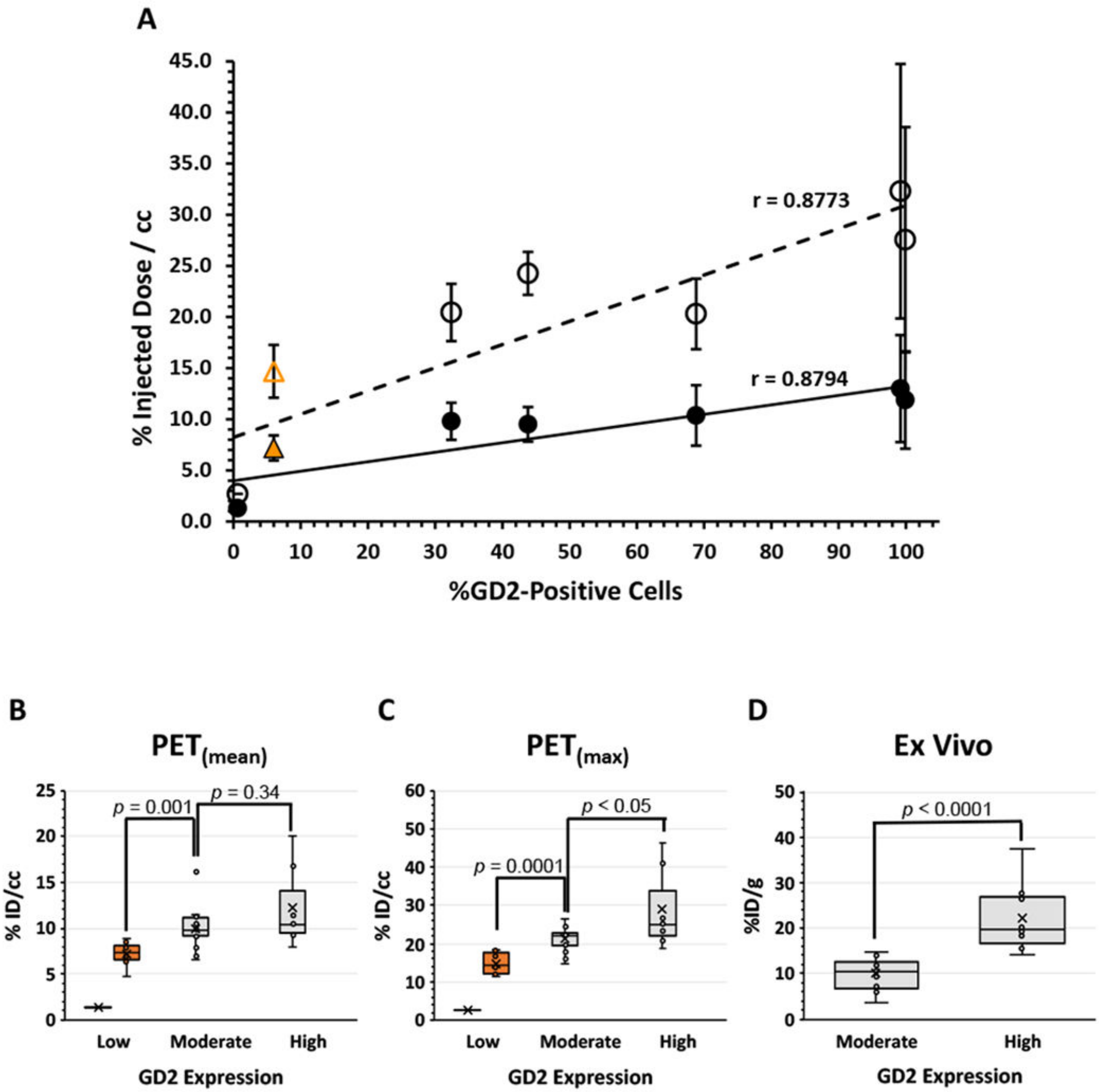

Figure 3.

Radiotracer accumulation *in vivo* can distinguish between tumors of low, moderate and high GD2 expression measured *in vitro*. Panel **A:** Correlation between % GD2-positive cells determined by flow cytometry and either mean (●) or maximum (○) tumor ^{64}Cu concentration determined by PET for 6 osteosarcoma PDX tumors, SJOS051 (n = 7), SJOS071 (n = 2), SJOS072 (n = 5), SJOS081 (n = 5), SJOS121 (n = 3) and SJOS845 (n = 1). Pearson correlation analysis demonstrated a strong relationship between PET signal and GD2 expression ($r = 0.88$, $p = 0.01$). The linear least squares regression line is also displayed for reference. The PET$_{(max)}$ and PET$_{(mean)}$ of tumors derived from the low GD2-

expressing osteosarcoma HOS cell line (n = 9) are presented here for comparison (orange △ and ▲, respectively) but as HOS is an immortalized cell line not a PDX, these data were not included in the correlation calculations. Panels **B** and **C** show the box-whisker plots of the mean (**B**) and max (**C**) tumor ^{64}Cu concentrations in the PDX tumors grouped as high (%ID/cc >99% GD2-positive cells, n = 7), moderate (32-69%, n = 15) and low (<1%, n = 1) GD2 expression measured as % GD2-positive cells by flow cytometry. The boxes represent the 25-75% quartiles with the median line indicated and the group mean represented by the “X”. HOS cell line tumors are included as a separate group (orange). Group continuous variables were compared through the Wilcoxon rank sum test implemented in SAS 9.4. A two-sided significance level of 0.05 was considered statistically significant. A statistically significant difference was observed between the high and moderate expression groups for the PET$_{(max)}$ data ($p < 0.05$) but not for the PET$_{(mean)}$ data ($p = 0.34$). The low expressing PDX was not included in the statistical analysis as this represents a single data point. However, a statistically significant difference was observed between the low-expressing HOS tumor group and the PDX moderate expression group for both PET$_{(max)}$ ($p = 0.0001$) and the PET$_{(mean)}$ ($p = 0.001$) data. Panel **D** shows the corresponding plot for the tumor radioactivity concentrations in these same PDX models measured by dissection and tissue radioactivity counting methods. These data confirmed the distinction between high (n = 10) and moderate (n = 19) GD2 expression ($p < 0.0001$). Dissection studies were not performed on the low-expressing SJOS845 PDX due to limited tissue availability.

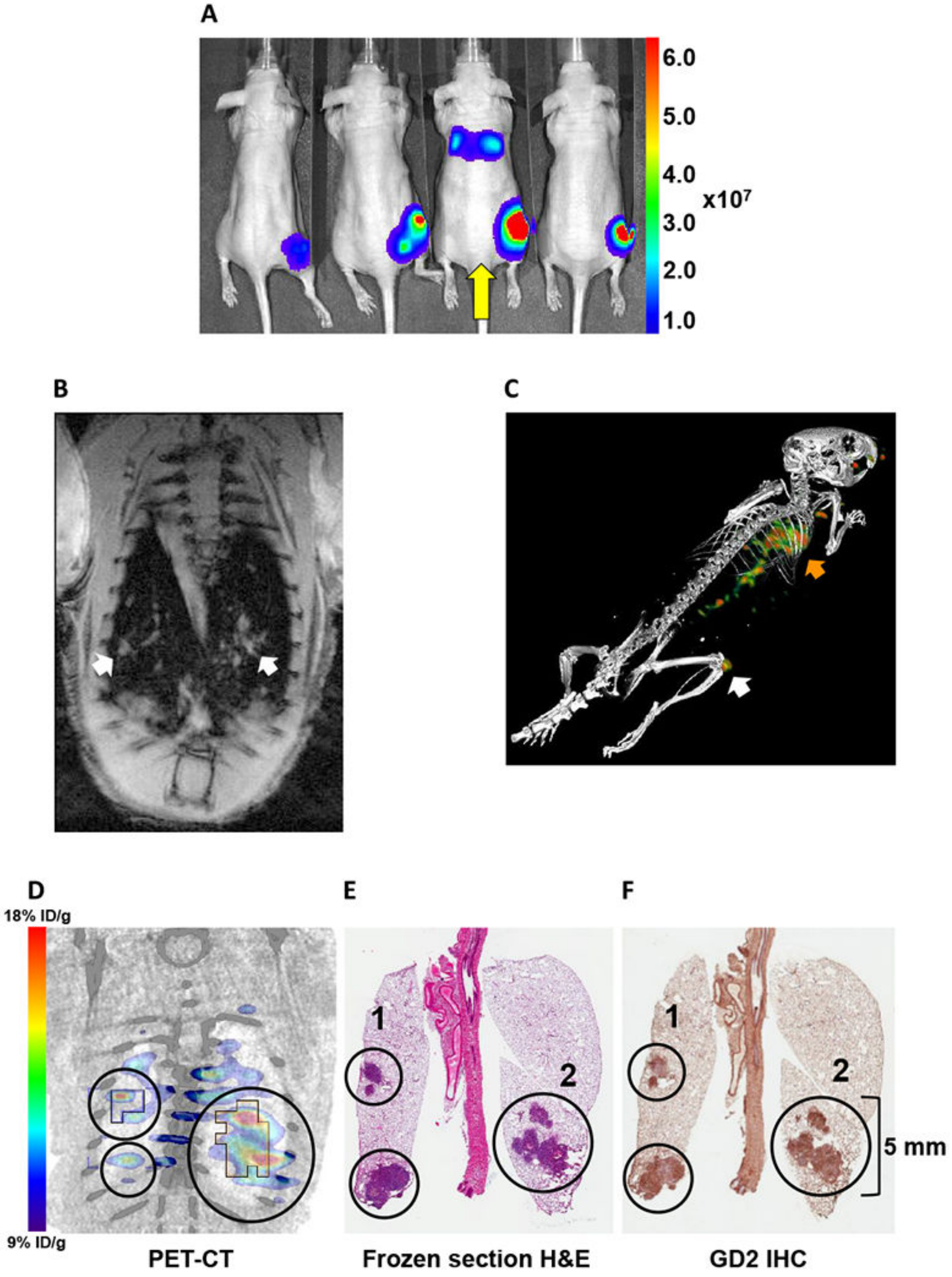

Figure 4.

Multimodality imaging demonstrates detection of GD2-positive lung metastasis. **A:** Bioluminescence imaging of luciferase-expressing 143B osteosarcoma tumor-bearing mice. Tumors at the site of femoral marrow implant were visible in 7 of 8 animals at 18 days post-implant. Mouse 3 (yellow arrow) was also positive for lung metastasis and was imaged by MRI the following day. **B:** Double-gated (respiration and cardiac), T1 weighted MR (7T) coronal image of the lungs of Mouse 3 at 19 days post-implant. White arrows indicate sites of high contrast suspicious for osteosarcoma. **C:** Fused static 3D PET-CT image of

[^{64}Cu]Cu-Bn-NOTA-hu14.18K322A accumulation in 143B tumor in nude Mouse 3 at 22 days after 143B cell injection in the distal right femur and 48 h after radiotracer injection. Primary tumor (white arrow) is from femoral marrow injection of 10^6 143B cells. The orange arrow indicates extensive metastatic invasion of lungs. **D-F:** Co-registered PET-CT and histopathology stains of metastatic 143B lung tumors. All lung lesions identified on PET also stained positive for GD2 (**F**) and demonstrated histology consistent with metastatic osteosarcoma (**E**). The upper-left region of interest (ROI 1) in each panel surrounds a readily discernable 29 mm^3 GD2-positive lesion. Both regions 1 and 2 (**D**) show $PET_{(mean)}$ [^{64}Cu]Cu-Bn-NOTA-hu14.18K322A accumulation of approximately 11 % ID/cc and $PET_{(max)}$ accumulation of approximately 20 % ID/cc. A summary of multimodality imaging and histology data for all eight animals in this study is tabulated in Supplementary Data Table S1.

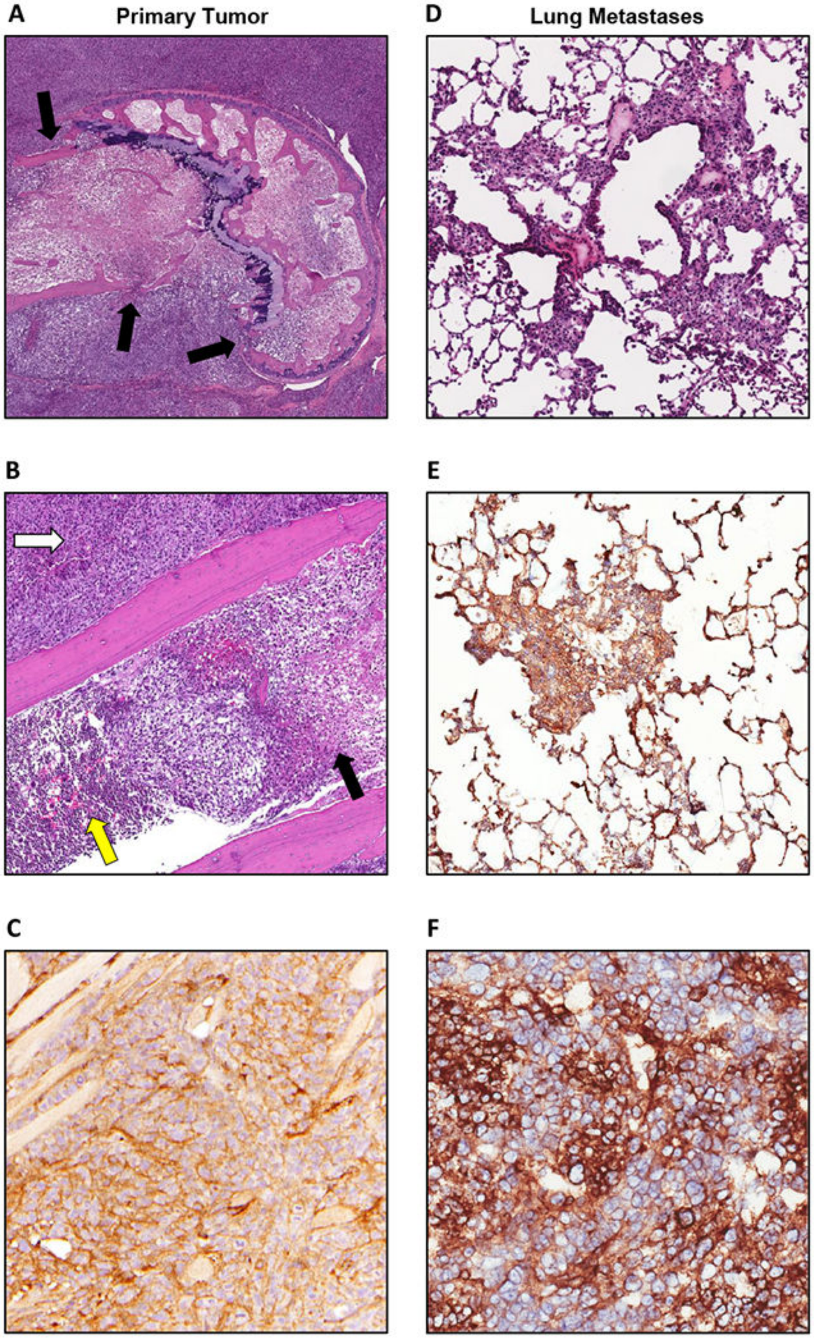

Figure 5.

Orthotopically implanted 143B osteosarcoma cells form GD2-positive lung metastases. Images from the primary orthotopic site (**A-C**) and lung metastases (**D-F**). **A:** H&E stain of 143B osteosarcoma cells implanted in the marrow cavity of the distal femur (5× magnification). Tumor cells have infiltrated through the cortical bone (black arrows) and out of the marrow cavity. **B:** H&E stain (20× magnification) showing areas of tumor cell infiltration and necrosis (black arrow) of marrow. Yellow arrow indicates area of unaffected bone marrow. Tumor cells also efface the adjacent skeletal muscle forming a bulky mass (white arrow). **D:** H&E stain (20× magnification) of mouse lung showing metastatic colonization of the lungs by tumor cells. GD2 staining of tumor cells (brown) counterstained with hematoxylin (blue) at the orthotopic site (**C**) was comparable to GD2 expression by tumor cells in the lungs (**E**, **F**).

Table 1.

Results of flow cytometry and IHC for GD2 expression compared with tumor radioactivity accumulation determined by PET and *ex vivo* dissection studies for 6 osteosarcoma xenografts and 4 osteosarcoma cell lines. The mean fluorescence intensity was calculated for the single, human, GD2-positive, live cells.

	IHC	**Flow Cytometry**		**$[^{64}Cu]$Cu-Bn-NOTA-hu14.18K322A**[b]		
Tissue	**GD2 Antibody (14.G2a)**	**% GD2-positive cells (14.G2a)**	**Mean fluorescence intensity**	**PET (max) % ID/cc**	**PET(mean) % ID/cc**	***ex vivo* % ID/g**
SJOS001105_X1 (SJOS051)	+	69	468	20 ± 3.4 (7)[c]	10 ± 3.0 (7)	8.3 ± 1.9 (5)
SJOS001107_X1 (SJOS071)	+	99	2691	32 ± 12 (2)	13 ± 5.2 (2)	24 ± 11 (5)
SJOS001107_X2 (SJOS072)	+	100	29,542	28 ± 11 (5)	12 ± 4.8 (5)	21 ± 5.0 (6)
SJOS001108_X1 (SJOS081)	+	32	3915	20 ± 2.8 (5)	9.8 ± 1.8 (5)	13 ± 1.5 (9)
SJOS001112_X1 (SJOS121)	+	44	604	24 ± 2.1 (3)	9.5 ± 1.7 (3)	6.2 ± 2.0 (5)
SJOS_TB 13-2845 (SJOS845)	−	<1	212	2.7 (1)	1.3 (1)	ND[a]
143B (cell line)	+	34	1218	29 ± 7.0 (7)	7.9 ± 2.2 (7)	ND
HOS (cell line)	ND[a]	6.5	3539	15 ± 2.6 (9)	7.2 ± 1.2 (9)	ND
U2OS (cell line)	ND	96	1445	ND	ND	ND
SaOS-2 (cell line)	ND	<1	30	ND	ND	ND

[a] ND = not determined

[b] Data represents the average (mean ± standard deviation).

[c] Number of animals per experiment shown in parenthesis (n).